

Dynamic contact angle of spreading droplets: Experiments and simulations

Cite as: Phys. Fluids **17**, 062103 (2005); <https://doi.org/10.1063/1.1928828>

Submitted: 13 October 2004 . Accepted: 19 April 2005 . Published Online: 26 May 2005

Š. Šikalo, H.-D. Wilhelm, I. V. Roisman, S. Jakirlić, and C. Tropea



View Online



Export Citation

ARTICLES YOU MAY BE INTERESTED IN

[Wetting effects on the spreading of a liquid droplet colliding with a flat surface: Experiment and modeling](#)

Physics of Fluids **7**, 236 (1995); <https://doi.org/10.1063/1.868622>

[Numerical studies of the influence of the dynamic contact angle on a droplet impacting on a dry surface](#)

Physics of Fluids **21**, 072102 (2009); <https://doi.org/10.1063/1.3158468>

[Drop impact and wettability: From hydrophilic to superhydrophobic surfaces](#)

Physics of Fluids **24**, 102104 (2012); <https://doi.org/10.1063/1.4757122>

AIP Conference Proceedings
FLASH WINTER SALE!

50% OFF ALL PRINT PROCEEDINGS

ENTER CODE **50DEC19** AT CHECKOUT



Dynamic contact angle of spreading droplets: Experiments and simulations

Š. Šikalo

Faculty of Mechanical Engineering, University of Sarajevo, Vilsonovo setaliste 9, 71000 Sarajevo, Bosnia and Herzegovina

H.-D. Wilhelm

Chair of Fluid Mechanics and Aerodynamics, Darmstadt University of Technology, Petersenstraße 30, 64287 Darmstadt, Germany and Siemens VDO, P AE RD, Sodener Straße 9, 65824 Schwalbach, Germany

I. V. Roisman, S. Jakirlić, and C. Tropea

Chair of Fluid Mechanics and Aerodynamics, Darmstadt University of Technology, Petersenstraße 30, 64287 Darmstadt, Germany

(Received 13 October 2004; accepted 19 April 2005; published online 26 May 2005)

This paper presents results of an experimental investigation of a single drop impact onto a dry, partially wettable substrate and its numerical simulation. Particularly, the drop spreading diameter and the dynamic contact angle are measured at different time instants after impact. Two surfaces, wax (low wettability) and glass (high wettability), are used to study the effect of surface wettability (static contact angle) on the impact dynamics. It is shown that existing empirical models for the dynamic contact angle (e.g., Hoffman–Voinov–Tanner law) do not predict well the change of the dynamic contact angle, especially at high capillary numbers. In addition to the experimental investigations, the drop impact was studied numerically, focusing primarily on the contact angle treatment. The singularity in the neighborhood of the moving contact line is removed from the computational domain and replaced by a local force with some dependence on the instantaneous advancing/receding contact-line velocity. The predicted time dependence of the drop spreading diameter and of the dynamic contact angle agrees well with the experimental data for both the advancing and receding phases of the impact process. © 2005 American Institute of Physics.

[DOI: 10.1063/1.1928828]

I. INTRODUCTION

The impact of a droplet onto a solid, dry surface is not only a process rich in fundamental hydrodynamics and physics but also is of large practical significance. Several reviews on the subject are available, dealing with a wide variety of impact conditions and surface properties.^{1–4} The drop deformation and its spreading on the wall is governed by inertial, viscous, capillary, and contact-line forces. This strongly in-stationary phenomenon (motion of several tens of meters per second is decelerated to zero within a few milliseconds) is affected also by the roughness of the impacted target^{5–11} and by the wettability of the substrate.^{11–18}

The study of these phenomena requires the development of theoretical models aimed to check the physical understanding of the problem (by comparison of the predictions with the experimental data) and to foresee the resulting outcome of the impact at asymptotic conditions (in our case high Reynolds and high Weber numbers). Most theoretical models of drop impact are based on a total energy balance of the impacting drop. These models are able to predict the maximum spread diameter.^{2,15,16} In a recent theoretical study¹⁹ the equations of motion of the rim bounding the radially expanding lamella are derived, accounting for, among other influencing factors, the changing (dynamic) contact angle. The model is able to predict well the temporal evolution of the drop diameter during the advancing and receding phases (on hydrophobic surfaces). This theory has also been

extended to the case of two-drop impacts,²⁰ reflecting applications associated with spray impingement.

The prediction of drop impacts at moderate or small Weber and Reynolds numbers (a case not so amenable to theoretical modeling) is an attractive application for numerical simulations. Although several problems are still unsolved, such as the prediction of the splash threshold or type of outcome,¹¹ numerical simulations have been successful.^{15,21–26} The first simulation, in 1967, using a marker and cell method (Harlow and Shannon²¹) to solve the Navier–Stokes equations, but neglecting viscous and surface tension effects, achieved satisfactory results for an impacting water droplet at the beginning of the spreading phase.

A finite element deformable grid for the drop was used in Ref. 15. They have taken into account the effects of viscosity, surface tension, and wettability with a good agreement between their experiments and simulations. Numerous studies^{17,22,23,26–29} showed the possibility of using the volume-of-fluid (VOF) method (Hirt and Nichols³⁰) to simulate drop impact onto a flat surface. For example, Bussman *et al.*²⁷ demonstrated the efficiency of the VOF method for studying the impact and spreading onto complex geometries and Fukai *et al.*¹⁵ onto various surfaces, stressing the effects of wettability. Most of the codes predict well the shape of the spreading drop during the time interval when the motion is dominated by inertia. The prediction of the receding phase of

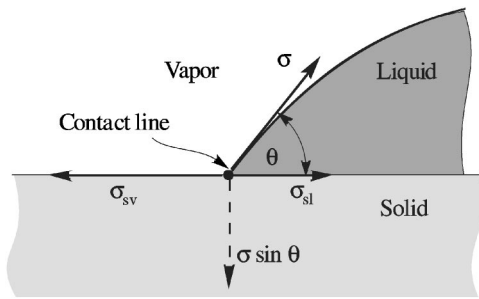


FIG. 1. Equilibrium wetting line and contact angle.

the drop (which is governed mainly by the capillarity and wettability) has not been as successful.

In both the theoretical and numerical treatment of this problem a boundary condition at the moving contact (or triple) line of the expanding droplet at the wall must be specified and, therefore, this phenomenon is closely related to the very large body of literature concerning wetting and dynamic contact lines. According to Young's equation

$$\sigma \cos \theta_e = \sigma_{sv} - \sigma_{sl}, \quad (1)$$

the static (equilibrium) contact angle θ_e is related to the surface tension of the solid/vapor σ_{sv} and solid/liquid σ_{sl} interfaces, as sketched in Fig. 1. The static contact angle is ideally a unique property of the material system being considered, but practically a hysteresis often arises depending on how the interfaces form. The advancing angle θ_a is the largest contact angle achievable before the wetting line begins to move in the direction of the gas phase and the receding angle θ_r is the smallest contact angle achievable before the wetting line begins to move in the direction of the liquid phase.

The contact angle is often determined experimentally using low-power optics at macroscopic scales (~ 0.01 mm) and is sometimes referred to as the apparent contact angle. The microscope contact angle is generally considered to be experimentally inaccessible.

The contact angle observed experimentally at a moving contact line is called the dynamic contact angle θ_D . It is this dynamic contact angle which is required as a boundary condition for modeling problems in capillary hydrodynamics, including certain stages of the drop impact problem. However, unlike the static contact angle, the dynamic contact angle is not a material property and at least for large capillary numbers, $Ca = v\mu/\sigma$, where v is the spreading velocity of the contact line and μ is the dynamic viscosity of the liquid, the macroscopic hydrodynamics will affect the dynamic contact angle. In fact, recent work indicates that this may be true for capillary numbers below unity.³¹

The angle formed between the liquid–vapor interface and the liquid–solid interface at the solid–liquid–vapor, three-phase contact line (or triple line) is conventionally defined as the *contact angle*. It should be noted that, at the molecular level, the three phases do not meet at a line but within a zone of small but finite dimensions in which the three interfacial regions merge. Therefore, the *microscopic* contact angle may be different from the contact angle measured by the method presented here. However, discussion of

such microscopic contact angles is beyond the scope of this work. A very detailed study of the interpretation of measured macroscopic contact angles can be found in Ref. 32.

The understanding of dynamic contact angles has progressed rapidly in recent years and a series of papers have introduced a rather unifying approach which treats the problem in more generalized framework of interface formation or disappearance.^{33–37}

Basically Young's equation is not abandoned; however, θ_e is replaced with θ_D , meaning either σ_{sl} or σ_{sv} must also vary with contact-line speed. A mutual interdependence of the dynamic contact angle and the flow field arises, something past approaches have not considered.

More classical approaches to the problem have focused on the so-called contact-line problem, referring to the shear-stress singularity resulting from the no-slip condition at the wall. An excellent overview of existing hydrodynamic approaches to the wetting phenomenon is given in the work of Shikhmurzaev (Ref. 35, Sec. 9).

One essential result relating the spreading velocity with the dynamic contact angle is obtained in the theoretical analysis of Cox³⁸

$$Ca = \left(\ln(\varepsilon^{-1}) - \frac{Q_1}{f(\theta_D)} + \frac{Q_2}{f(\theta_w)} \right)^{-1} [g(\theta_D) - g(\theta_w)] + O\left(\frac{1}{\ln(\varepsilon^{-1})} \right)^3, \quad (2)$$

where θ_D is the macroscopic (dynamic) contact angle, θ_w is the wall (microscopic) contact angle usually associated with the equilibrium angle θ_e , Q_1 and Q_2 are constants associated with the outer flow and with the wall slip, ε is a small dimensionless parameter associated with the microregion of the contact line, $f(\bullet)$ and $g(\bullet)$ are functions obtained in Ref. 38. The study is based on the creeping velocity field in the corner³⁹ and is thus valid for both spreading and receding cases.

All existing empirical models of the dynamic contact angle are simplifications of the general expression (2). The most widespread working relation describing the contact angle is given by the so-called Hoffman–Voinov–Tanner law for small Ca ,

$$\theta_D^3 - \theta_e^3 \cong c_T Ca, \quad (3)$$

where c_T is a constant given by Hoffman⁴⁰ to be about 72, with some dependence on the flow system size.

Hoffman⁴⁰ deduced a universal function from a systematic study of dynamic contact angles in glass capillary tubes for a wide range of capillary numbers ($4 \times 10^{-5} < Ca < 36$). Hoffman did not provide an explicit mathematical form for the function $\theta_D(Ca)$. Jiang *et al.*⁴¹ give an empirical correlation which fits the data equally well,

$$\frac{\cos(\theta_e) - \cos(\theta_D)}{\cos(\theta_e) + 1} = \tanh(4.96 Ca^{0.702}). \quad (4)$$

In both cases the dynamic contact angle increases with flow velocity and asymptotically reaches 180° for high capillary numbers. Several additional empirical correlations^{42,43} are obtained using the experimental data for solid strips

TABLE I. Properties of the liquids and wettability of the surfaces.

Liquid	σ (N/m)	μ (mPa s)	ρ (kg/m ³)	$\theta_a - \theta_r$	
				Glass	Wax
Water	0.073	1.0	996	10°–6°	105°–95°
Glycerin	0.063	116	1220	17°–13°	97°–90°

dipped a pool at low capillary numbers ($0.002 < Ca < 0.02$). However, no dependence on the flow field is presumed.

A more recent empirical correlation for the dynamic contact angle is given by Kistler⁴⁴ in the form

$$\theta_D = f_{\text{Hoff}}[Ca + f_{\text{Hoff}}^{-1}(\theta_e)], \quad (5)$$

where $f_{\text{Hoff}}^{-1}(\bullet)$ is the inverse function of the “Hoffman’s” function $f_{\text{Hoff}}(\bullet)$ defined as

$$f_{\text{Hoff}}(x) = \arccos \left\{ 1 - 2 \tanh \left[5.16 \left(\frac{x}{1 + 1.31x^{0.99}} \right)^{0.706} \right] \right\}. \quad (6)$$

Returning to the case of drop impacts onto solid surfaces, the expanding lamella during drop spreading or the receding lamella during drop recoiling for nonwetting systems^{18,45} offers not only an interesting situation to study the behavior of the dynamic contact angle, but also a correct treatment is essential for predicting the outcome of the impact. The present study experimentally investigates the dynamic contact angle during drop impact onto horizontal surfaces. Comparisons with existing theories are given. Next, the numerical simulations of drop impact are performed, accounting for the dynamic contact angle variation with the instantaneous spreading velocity. A newly proposed algorithm improves significantly the precision of the predictions of the temporal evolution of the drop diameter and the apparent contact angle. In this study two dynamic contact angles are distinguished.

The first angle is the contact angle θ_D which is observed in the experiments. The value of this angle changes during drop spreading and can be predicted from the drop shape in the numerical simulations. In the following text this angle is called the *apparent dynamic contact angle*.

The second angle is the angle θ_{Di} in the inner viscous region near the contact line. In our experiments the length of this viscous region can be much smaller than the size corresponding to one pixel of the drop image. This length is also much smaller than the mesh size in the numerical simulations. Therefore, the inner viscous region is not observed in our experiments and cannot be calculated in our numerical simulations. The value of θ_{Di} is related to the local viscous drag near the moving contact line and therefore determines the evolution of the contact line. In this study the value of the angle θ_{Di} is assumed to be function of the equilibrium contact angle and the capillary number. It is predicted using the empirical model (5).

II. EXPERIMENTAL TECHNIQUES AND CONDITIONS

To investigate the apparent dynamic contact angle of impacting liquid droplets, a series of experiments were conducted with individual droplets impacting onto solid, dry, and smooth surfaces. The experimental method has been previously described in Ref. 45.

A high resolution charge-coupled device (CCD) camera (Sensicam PCO, 1280×1024 pixels) equipped with a long-distance microscope is used to observe the spreading droplet in detail. The magnification was manipulated so that the image could accommodate the maximum spread of the droplet. The spatial resolution (number of pixels per millimeter) was calibrated using a calibration scale. For example, at the scale of 213 pixel/mm one pixel resolution corresponds to $4.7 \mu\text{m}$. From the side-view images, the spread factor and the apparent dynamic contact angle are measured.

In the present study experimental data on the apparent dynamic contact angle of a glycerin/water mixture (85% of glycerin) droplet and a distilled water droplet ($D = 2.45 \text{ mm}$) spreading on a horizontal surface are presented. The physical properties of the liquids and the wettability of the surfaces (advancing θ_a and receding θ_r contact angles) are shown in Table I. The drop’s initial diameter is the same for all the experiments whereas the impact velocity ranges from 1 to 4.1 m/s. The list of impact parameters is given in Table II.

The visualization method presented here also allows a measurement of the contact angle. The values of apparent dynamic contact angles may be appreciably larger (advancing) or smaller (receding) than corresponding static values. Superficially, the contact angle is the angle between the tangent to the droplet’s profile and the tangent to the surface at the intersection point of gas, fluid, and solid, as Fig. 2 shows. The difficulty is in accurately estimating the tangent to the curved droplet profile because the curve ends at the point where one needs to measure it. This technique requires having the droplet in focus and having a clear base line. Also the results are sensitive to the viewing angle. It can have a significant impact of the clarity of the base line and base line errors can introduce contact angle errors of several degrees. In the experiment the camera was placed horizontally.

In this technique a tangent is simply aligned with the spreading-droplet profile at the point of contact with the solid surface. This is done directly using image processing software (OPTIMAS 6.2), which allows the measurement of line inclination. The results are somewhat subjective and depend on the experience of the operator, although certain training

TABLE II. List of experiments. The initial drop diameter is 2.45 mm in all the experiments.

Experiment	Liquid	Wall	Impact velocity (m/s)	We	Re
Expt. 1	Glycerin	Wax	4.1	802	106
Expt. 2	Glycerin	Glass	4.1	802	106
Expt. 3	Glycerin	Wax	1.41	93	36
Expt. 4	Glycerin	Glass	1.41	93	36
Expt. 5	Glycerin	Wax	1.04	51	27
Expt. 6	Glycerin	Glass	1.04	51	27
Expt. 7	Water	Wax	1.64	90	4010

procedures can be used to improve both the accuracy and precision. The accuracy is enhanced by the use of sharpening of images, which permits the detailed examination of the intersection of the droplet profile and the solid surface. The tangent is aligned to the droplet profile at the point of contact with the solid. With some training, this method of measurement of droplet contact angles can rapidly yield results exhibiting a repeatability of $\approx \pm 5^\circ$.

III. NUMERICAL SIMULATIONS OF DROP IMPACT

A. Computational method

In parallel to the experiments, numerical simulations of the droplet impact using the VOF-based free-surface capturing method⁴⁶ were performed. The free-surface capturing method takes into account the interaction between the liquid and the gas, and it is basically a two-phase model, which assumes that both phases share the same velocity field, and as such it is well suited for nonmixing fluids. This makes an important difference between this and the classical VOF method.

The computational method involves the solving of an equation describing the conservation of volume concentration C simultaneously with the equations governing mass and momentum; the latter equation accounting for the surface tension (capillary) forces in addition to the pressure, viscous, and gravity forces. The volume concentration (fraction) C is defined as a ratio between the volume occupied by the liquid and the total volume, taking the value 0 in the air and the value 1 in the liquid. Hereby, the free surface (0

$< C < 1$; the value $C=0.5$ defines its actual position) is captured within a few grid cells, representing actually a transition region of finite thickness. Two immiscible fluids are treated as one effective fluid in the whole solution domain, having its physical property dependent on the distribution of the volume concentration and the properties of the actual fluids. As in the real case, the physical properties (density and viscosity) take constant values within each fluid, but will vary across the free surface.

In the computational model applied here,⁴⁶ the volumetric force f_σ associated with surface tension is expressed in terms of the volume concentration C via the vector normal to the free surface (∇C) in the framework of the so-called continuum surface force (CSF) model proposed by Brackbill *et al.*:⁴⁷

$$f_\sigma = \sigma \left[- \nabla \cdot \left(\frac{\nabla C}{|\nabla C|} \right) \right] \nabla C. \quad (7)$$

The term in brackets represents the mean curvature κ of the interface. Since the gradient of the volume concentration is nonzero only in the vicinity of the free surface, the volumetric force f_σ acts only in this transition region.

The discretization of the convective part of the volume fraction conservation equation needs special attention. Ideally, its discretization should neither produce numerical diffusion nor unbounded values of the volume fraction, i.e., the values of the volume fraction in each cell should lie between the minimum and maximum value of the neighboring cells. The demand for a scheme to be bounded implies that the computed fluxes of volume fraction do not underflow or overflow the cells. In the present work the high resolution interface capturing (HRIC) scheme⁴⁶ is used for discretization of the volume concentration convective fluxes. The scheme is a nonlinear blend of upwind and downwind cell-face values, based on the spatial distribution of the volume concentration, the local Courant number ($Co = u\Delta t/\Delta x$), and the angle between the normal to the interface and the cell-face surface vector. Furthermore, an implementation of the HRIC discretization scheme to unstructured grids is simple and straightforward, while the classical VOF discretization of the volume fraction depends very much on the cell and grid topologies.

All computations were performed by the multipurpose computer code COMET (Ref. 48) based on a finite volume numerical method for solving three-dimensional, Navier–

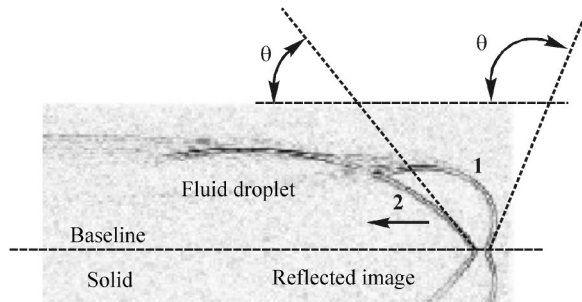


FIG. 2. Contact angle measurements for a glycerin droplet on smooth wax. Exposure 1 taken in an early recoiling phase ($\theta \approx 111^\circ$) and exposure 2 taken in the recoiling phase $\theta \approx 51^\circ$. ($D=2.45$ mm, $We=802$, time between the exposures is $\Delta t=6.72$ ms.)

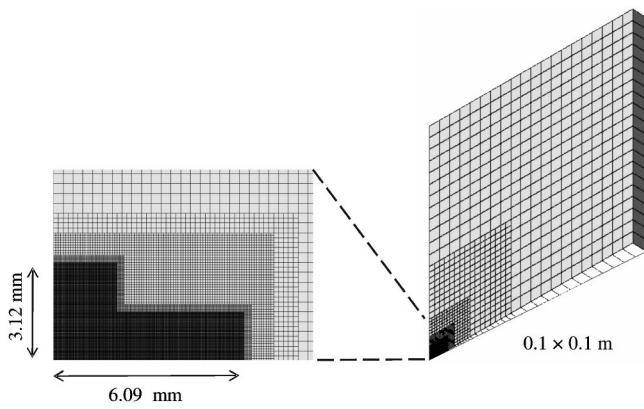


FIG. 3. Blowup of numerical grid used for the computations, showing regions of gradual refinement.

Stokes equations using a cell centered (collocated) variable arrangement and allowing the discretization of the governing equations on fully unstructured grids. The primary variables are the velocity and pressure. The velocity-pressure coupling is ensured by the pressure-correction method based on the SIMPLE algorithm. Diffusion fluxes are approximated by central differences. A blended upwind-central differencing scheme in the so-called differd-correction manner was used (the contribution of central differencing scheme was 100%) for the discretization of convective terms in all transport equations. Here the second-order, three time levels, fully implicit scheme was used for time discretization.

B. Numerical grid

With the exception of small capillary waves on the drop surface and along the rim appearing at the edge of the radially expanding lamella, the normal drop impact could be considered as axisymmetric. Sample three-dimensional (3D) simulations (not presented here) completely agree with the computations of normal drop impact using the 2D axisymmetric grid. The computational domain had the shape of a cylindrical pie slice consisting of only one control volume in the azimuthal direction, enabling 2D computations in a cylindrical coordinate frame on a fixed nonuniform grid, Fig. 3.

The solution domain represents a $100 \times 100 \text{ mm}^2$ large square in the r - z plane. The liquid drop occupies only the refined part of the grid in the lower left corner, as can be seen in the blow-up of the numerical grid in Fig. 3 (left). All control volumes are squares in the r - z plane. The smallest grid cells are $19.5 \text{ }\mu\text{m}$. This corresponds to the criterion that with the VOF method, typically three to four control volumes must be contained in the region between two free surfaces, such as in the case of the splashing lamella.⁴⁹ With extensive use of nonuniform, unstructured grids and refinement only in the region of drop movement, the grid has in total less than 40 000 cells. In an early stage of this study, grid dependence tests were also performed (the finest grid used had 141 000 cells with a minimum size of $10 \text{ }\mu\text{m}$). These tests confirmed that the grid selected for later parametric studies were sufficiently fine, yielding an estimated discretization error smaller than 1%.

To decrease calculation time without interfering with sta-

bility, the size of the next time step Δt was computed before every new time step. The time step is calculated for a fixed value of the Courant number ($Co=0.2$) and the variable local velocity in the cells containing liquid ($C>0.5$). The smallest value of the time step calculated, corresponding to the maximum velocity $u_{i,\max}$ found in the grid cells of interest, is implemented, so that the actual local Courant number will always be less than or equal to 0.2,

$$\Delta t_{\text{new}} = 0.2 \frac{\Delta y_{\min}}{u_{i,\max}}, \quad (8)$$

where Δt_{new} is the time step currently calculated and Δy_{\min} is the length/dimension of the smallest cells of the grid. The resulting time step was of the order of 10^{-4} ms – 10^{-3} ms .

C. Physical interpretation of the dynamic contact angle and its implementation

The main feature of the numerical computations to be discussed in the present paper is the simulated physics associated with the contact-line movement and the related (dynamic) contact angle. The implementation of the boundary condition related to the dynamic contact angle is explained in the following section. The conventional averaging of the momentum of the flow inside a numerical cell is not valid in the neighborhood of the contact line. The cell including this contact line consists of two main regions at different distances from the contact line (see Fig. 4): the “outer” region where the inertia is not negligible; the “inner” region, near the corner, where inertia is negligibly small, the stresses and thus the curvature of the free surface are singular at the contact line.

In order to simulate all the details of the flow near the contact line, including the flow and the geometry in the inner region, the size of the mesh in this region should be of the order of the “slip length” ε . This length is comparable with the intermolecular distances and is significantly smaller than the typical drop size. Any mesh of size larger than ε will lead to the mesh size dependent results. On the other hand, the accurate direct numerical computation of the flow with the moving contact line using the extremely fine mesh of the size ε could require enormous computational resources.

We have chosen an alternative and more efficient approach of matching the computed flow in the “outer region” with the theoretical results for the singular “inner region” [Figs. 4(b)–4(d)]. In Fig. 4(c) the contour plot of the stream function of the creeping flow³⁹ in the corner is shown. The inner region has a characteristic size $R_i \ll \mu/\rho v_{cl}$. The characteristic size R_o of the outer region depends on the macroscopic flow in the droplet. Three typical smallest distances from the contact line can be distinguished in the outer region: $R_{o1} = \nu/|v_{cl}|$ at which the inertial effects become significant; $R_{o2} = \nu^{1/2}|v_{cl}|^{1/2}|dv_{cl}/dt|^{-1/2}$ at which the influence of the acceleration dv_{cl}/dt becomes significant; $R_{o3} = |v_{cl}\gamma|^{-1}$ at which the influence of the gradient γ of the macroscopic velocity field becomes significant.

The characteristic radius R_o can be thus determined as $R_o = \min(R_{o1}, R_{o2}, R_{o3})$. Consider, for example, a 3 mm glycerin drop impacting with the velocity of 4 m/s. The typical

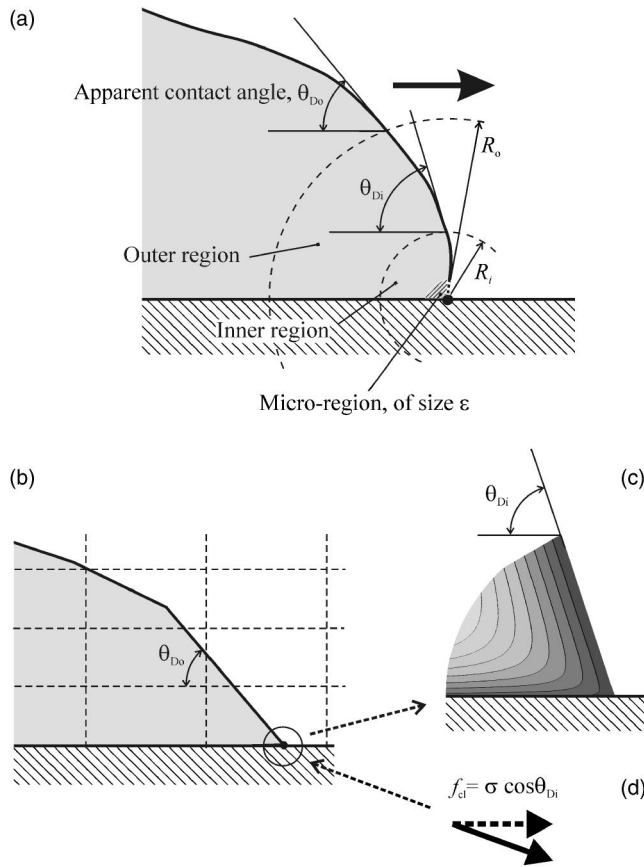


FIG. 4. Sketch of the area near the contact line. (a) Definition of contact angles and regions, (b) computation scheme with the excluded singular, inner region, (c), and substituted by a distributed force $f_{cl} = \sigma \cos \theta_{Di}$ (d).

sizes of the outer region of the contact angle are $R_{o1} \sim 30 \mu\text{m}$, $R_{o2} \sim 300 \mu\text{m}$. R_{o3} is comparable with the thickness of the lamella. The mesh size should be comparable with R_o in order to account for the inertial effects in the corner near the contact line.

In the present numerical scheme, the size of the mesh is much larger than the characteristic size R_i of the inner region. This entire inner region is removed from the computational domain and substituted by an additional force per unit length, f_{cl} , applied to the contact line. Because the inertial effects are negligibly small here, this force balances the capillary force and the viscous drag applied to the inner region. This force is normal to the contact line, i.e., parallel to the wall (in the radial direction for the axisymmetric case). The magnitude of this distributed force is defined as

$$f_{cl} = \sigma \cos \theta_{Di}, \quad (9)$$

where θ_{Di} is the angle between the free surface and the wall at the outer boundary of the inner region: actually it is the dynamic contact angle described by the Hoffman's law or by the theoretical solutions based on creeping flow in the neighborhood of the contact line. The outer region considered in Cox³⁸ is much smaller than the mesh size and corresponds to our inner region defined in Fig. 4. Following this study the contact angle θ_{Di} is a function of the capillary number $Ca = \mu v_{cl} / \sigma$ and the static contact angle θ_e . This dependence is expressed in Eq. (2).

The asymptotic expression (2) is valid only for very small capillary numbers ($Ca \ll 1$). It agrees well with the empirical relations (4) and (5). This means that the choice of the model for the contact angle should not significantly influence the computational results. In the present model we have used the recent model⁴⁴ given in Eq. (5). Because the inertia in the inner region is negligibly small, the same expression (5) is used for both spreading ($Ca > 0$) and receding ($Ca < 0$), as was concluded in Ref. 38. In our case two limiting values for the static contact angle are used: the advancing (spreading) or receding contact angle, θ_a or θ_r , depending on the sign of the velocity v_{cl} of the contact line.

The velocity v_{cl} of the contact line is not a material velocity and cannot be easily extrapolated by the velocity field in the outer region belonging to the computational domain. This velocity is obtained by numerical differentiation of the radius r_{cl} of the wetted spot on the wall: $v_{cl} = dr_{cl} / dt$.

The apparent contact angle θ_{Do} at the outer region differs from the inner angle θ_{Di} because it accounts for the inertial effects in the outer region.

The boundary condition (9) in the region around the contact line can be easily incorporated within the framework of the CSF model. The volumetric force f_σ applied to the numerical cells in this region is calculated with the help of (7) using the local distribution of C and setting the unit normal vector to the contact line as follows:

$$\left(\frac{\nabla C}{|\nabla C|} \right) = \mathbf{n}_{\text{wall}} \cos \theta_{Di} + \mathbf{n}_{cl} \sin \theta_{Di}, \quad (10)$$

where \mathbf{n}_{wall} is the unit normal vector directed into the wall and \mathbf{n}_{cl} is the unit vector parallel to the wall. The value of the dynamic contact angle θ_{Di} is computed from (5) for each time step. It is important to note that we do not *prescribe* the apparent dynamic contact angle θ_D in our numerical scheme, but only the force f_{cl} associated with viscous drag and capillary effects in the corner. The apparent contact angle accounts also for the inertial effects; it can differ from θ_D and represents actually the result of our simulations.

It is worthy to note that the contact angle of the stationary contact line is equal to the equilibrium one:

$$\lim_{Ca \rightarrow 0} \theta_{Di} = \theta_e.$$

The corresponding distributed force becomes $f_{cl \text{ static}} = \sigma \cos \theta_e$, which coincides with the corresponding resulting force $f_{cl \text{ static}} = \sigma_{sv} - \sigma_{sl}$ (Fig. 1) and leads to the correct static shape of the drop with the contact angle $\theta = \theta_e$.

IV. RESULTS AND DISCUSSION

A. Experimental results

From the experiments two geometric parameters of the spreading drop have been measured. One of these is the spread factor, which is the diameter of the wetted spot on the wall surface nondimensionalized by the initial, undisturbed drop diameter upon impact. The second parameter is the apparent dynamic contact angle.

In Figs. 5–7 the experimental results for the spread factor and for the apparent dynamic contact angle are shown as

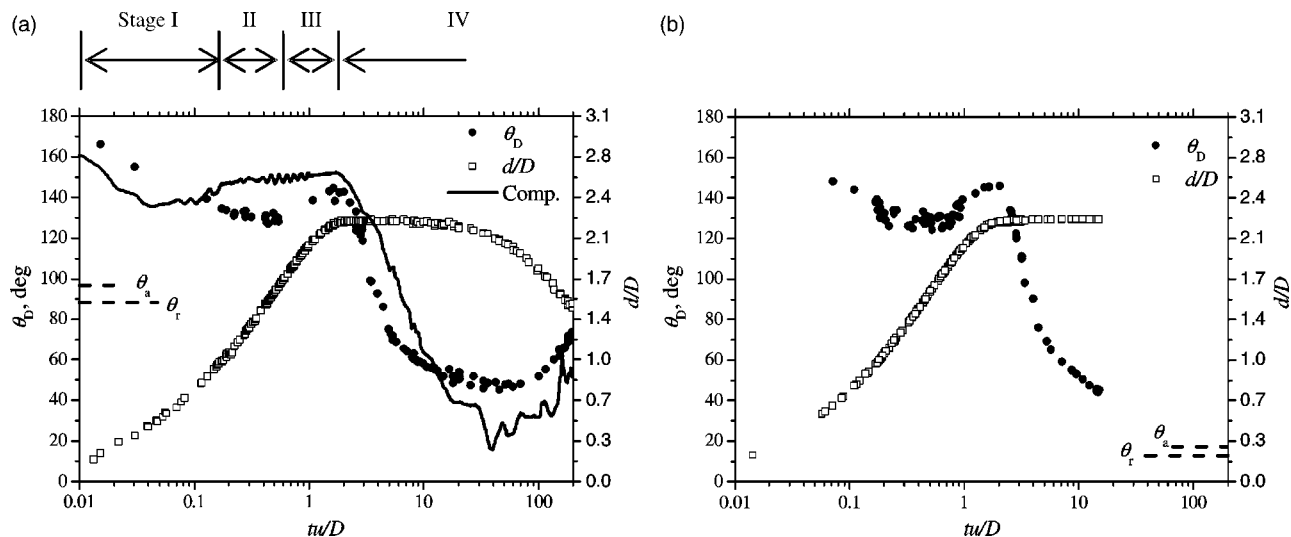


FIG. 5. Dynamic contact angle and spread factor of a glycerin droplet on (a) smooth wax and (b) smooth glass: expt. 1 and expt. 2 from Table II.

functions of time for various impact velocities (Weber numbers are 802, 93, and 51). The results correspond to the impact of a drop onto smooth wax (with a relatively high static contact angle) or glass (of small static angle) substrates. The values of the advancing and receding static contact angles are also marked in the figures.

The general behavior of the apparent dynamic contact angle is similar for all the considered cases. The typical stages of such behavior are shown in Fig. 5(a). During the initial phase of spreading, (stage I) the wetting angle decreases to a local minimum of about 130° for a glycerin droplet (stage II). During the following spreading phase (stage III) the apparent dynamic contact angle increases to a local maximum of about 150° . The apparent contact angle of a glycerin droplet reaches its maximum value at about the same time as the spread factor. The apparent dynamic contact angle then decreases rapidly from its maximum value (stage IV), which is significantly larger than the static value.

On the wax surface the apparent dynamic contact angle may fall below its static value, coinciding with the recoiling of the droplet observed at higher impact velocities. At low

Weber numbers no recoil is observed, although the last measured values of the apparent dynamic contact line lie below the static values. In these cases a relaxation to the static value is observed over much larger time scales than those observed in these experiments. In Fig. 5(a) the apparent dynamic contact angle remains almost constant at its maximum value $\sim 130^\circ$ in the time interval $2 < tu/D < 20$. Such a behavior is predicted in the theoretical model of Ref. 19 and corresponds to the value of the contact angle in the inner region, being in the range $\theta_r < \theta < \theta_a$. The apparent contact angle is determined by the flow in the drop.

For impact onto glass the apparent dynamic contact angle decreases rapidly from its local maximum but then shows signs of asymptotically approaching its static values, while the spread factor remains constant, Fig. 5(b). The rate of asymptotic approach appears to be significantly faster for higher Weber numbers.

In Fig. 8 the apparent contact angle during stages I and II is considered in detail. At the range of the spread factors less than 0.8, the apparent contact angle is independent of the impact parameters and of the properties of the substrate.

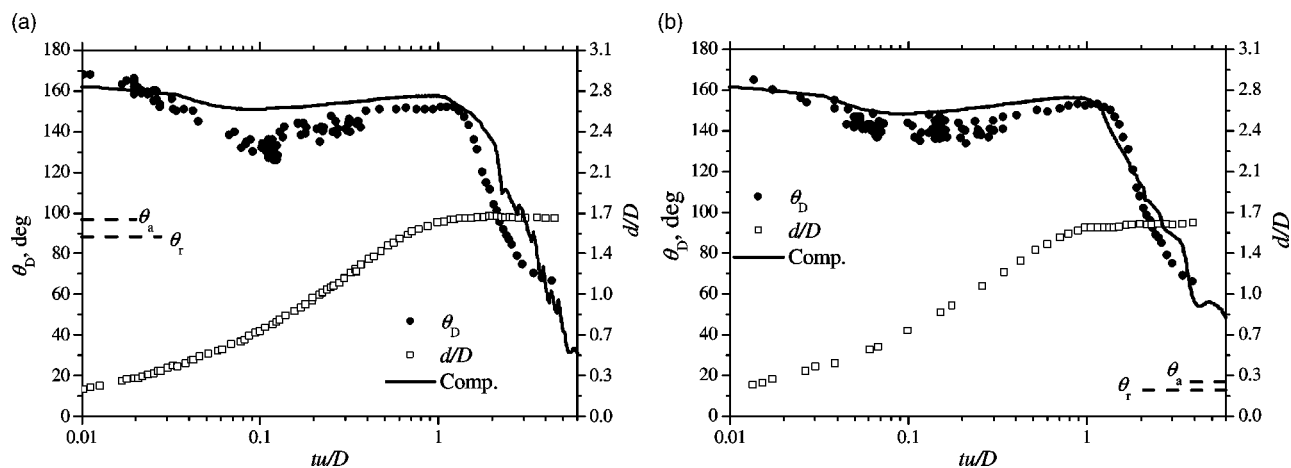


FIG. 6. Dynamic contact angle and spread factor of a glycerin droplet on (a) smooth wax and (b) smooth glass: expt. 3 and expt. 4 from Table II.

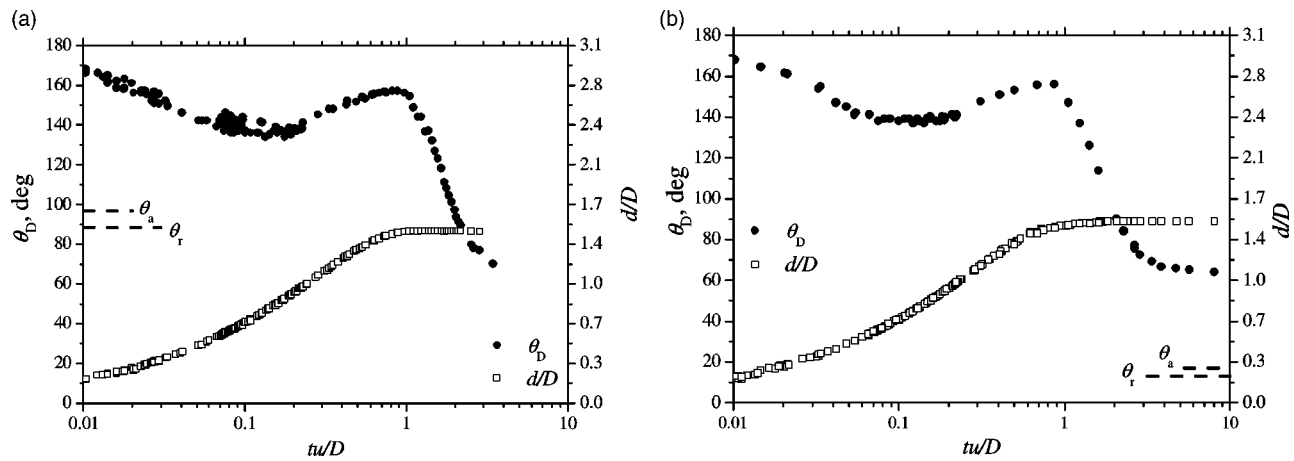


FIG. 7. Dynamic contact angle and spread factor of a glycerin droplet on (a) smooth wax and (b) smooth glass: expt. 5 and expt. 6 from Table II.

Moreover, during this kinematic phase of spreading¹⁸ the drop shape can be approximated by a truncated sphere moving with the constant velocity towards the substrate. The deformation of the drop takes place in a very thin region near the wall. The apparent contact angle during this stage can be approximated by the angle between the spherical surface with a plane of the substrate. Such approximation, $\theta_D = \pi/2 - \arccos d/D$, as shown in Fig. 8 with a dashed line, agrees rather well with the experimental data in the range $0 < d/D < 0.8$ for all the impact parameters.

At some time instant the apparent contact angle reaches a minimum value of $\approx 130^\circ$. It is known that the inertial effects in the flow near the contact line are minor at very small distances from the triple line and at small propagation velocities v_{cl} . However, the motion of the contact line at angles above $\sim 128.7^\circ$ leads to the appearance of vortices in the creeping flow in the corner.³⁹ The inertial effects become significant and the flow in the neighborhood of the contact line is influenced mainly by the outer flow. These theoretical predictions are confirmed by the appearance of the stage II with constant contact angle of $\approx 130^\circ$. The behavior of the

apparent dynamic contact angle in the range $\theta_D > 128^\circ$ cannot be accurately described by existing theoretical or empirical models based on creeping flow in the corner because a unique solution does not exist.

Next, after the reaching of the local minimum of $\sim 130^\circ$, the apparent contact angles in Fig. 8 begin to increase again as the spread factor grows (stage III). This increase begins later for the higher impact velocities. It does not depend on the substrate (the experimental results for the same impact parameters but different substrates coincide almost completely). The capillary number at this stage is very large. This means that the influence of capillary forces on the value of the contact angle is negligibly small. Hence, the increase of the contact angle during the stage III is caused by the viscous stresses initiating the “rolling motion” in the corner. Therefore, the beginning of the stage III occurs later for the “less viscous” drop impacts of higher Reynolds number.

In order to analyze the experimental results at the later stages of spreading and to evaluate empirical models, the data for the apparent dynamic contact angle are shown in Fig. 9 as a function of the capillary number ($Ca = v_{cl}\mu/\sigma$) in comparison with the existing correlations.^{41–44} The velocity of propagation of the contact line v_{cl} is calculated by differentiating the spread factor in time. It should be noted that the higher values of the capillary number in these graphs correspond to the initial stage of the impact whereas the small capillary number corresponds to the later phase of the advancing contact line. The cases of glycerin drop impact onto smooth glass [Fig. 9(a)] and wax [Fig. 9(b)] substrates are shown. It can be clearly seen that the contact angle reaches a local maximum at approximately $Ca \approx 0.1$. The decreasing of θ_D during the beginning of the stage IV (characterizing by the small capillary numbers $Ca < 0.1$) is thus caused by the surface tension and the forces associated with the wettability.

As expected, the empirical correlations are closer to the experimental data for the apparent dynamic contact data only at a very small capillary number ($Ca < 0.1$). At larger velocities the inertial effects in the contact corner become significant and the models, predicting the values of the apparent dynamic contact angle in the neighborhood of $\theta_D \rightarrow \pi$, are no longer valid. Actually, these empirical correlations are devel-

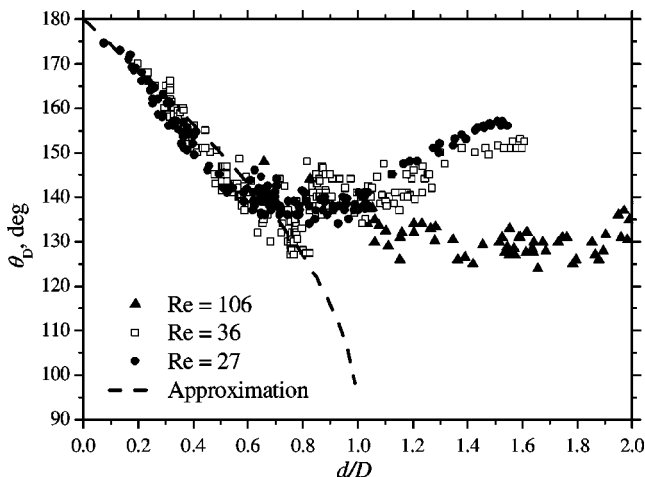


FIG. 8. Dynamic contact angle during the initial phase of spreading ($tu/D < 1$) as a function of the spread factor for $Re=106$ (expt. 1 and expt. 2 from Table II); $Re=36$ (expt. 3 and expt. 4); $Re=27$ (expt. 5 and expt. 6). The approximation is $\theta_D = \pi/2 - \arccos(d/D)$.

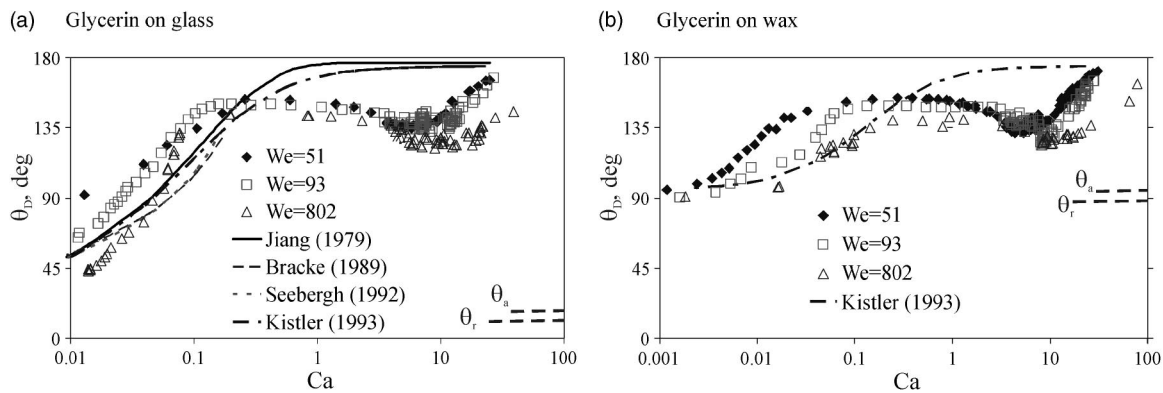


FIG. 9. Data for the apparent dynamic contact angle θ_D vs Ca for glycerin droplet on (a) smooth glass and (b) wax, in comparison with the empirical correlations (Refs. 41–44).

oped and valid only for very small capillary numbers and zero acceleration. For lower capillary numbers ($Ca < 0.1$) shown in Fig. 9, the apparent contact angle is larger for drop impacts with smaller impact velocity (smaller Weber number).

The irregular behavior of the data has been noted previously by Blake⁵⁰ for a tape vertically entering into a pool of water (see the work by Blake and Ruschak,³¹ Figs. 3.17 and 3.20, pp. 82–84). Blake's results exhibit the change in the slope of the data at much lower values of Ca . The data have a negative slope at Ca above about 2.7×10^{-5} ($v \sim 0.002$ m/s). The slope is again positive at Ca above about 0.007 ($v \sim 0.5$ m/s).

The discrepancy between the theory and experimental data in Fig. 9 can be explained by the importance of the inertial effects associated with the velocity and acceleration of the contact line already at the length scale comparable with the size of 1 pixel of the image. The macroscopic flow field far from the contact line also influences significantly the contact angle at some characteristic distance from the triple line.

Note, however, that the theoretical analysis⁵¹ of the inertial and viscous effects on the flow near the high velocity contact line yields a modified expression for the dynamic contact line in a form similar to (2), where the dynamic contact line is a function of the capillary number only. In the present study the inertial effects, associated with these factors, are accounted for using the numerical solution for the velocity field in the outer region (see Sec. III C). In the following section the results of the numerical simulations of drop impact are given.

B. Validation of the numerical code

Two criteria were used to compare the experimental and numerical results: a qualitative comparison of the drop shape at several time instants after the impact was performed; a quantitative comparison was made for the values of the spread diameter (diameter of the contact area between the liquid and the solid) and the macroscopic, apparent dynamic contact angle of the drop during the impact process.

A qualitative comparison of the droplet shapes obtained by simulation and the images of the deforming drops ob-

tained using a CCD camera is shown in Figs. 10 and 11. The time sequence of the spreading drop is shown in Fig. 10 whereas the time sequence of the receding is shown in Fig. 11.

After contact with the solid surface, the lower part of the droplet compresses and deforms. A liquid sheet (lamella) ejects close to the contact line and spreads over the solid surface. At the beginning, the thickness of the lamella is smaller than $6 \mu\text{m}$, which is $\approx 5 \times 10^{-3}$ of the initial drop diameter. Therefore, in order to capture the entire process a very fine grid has been chosen for the simulations (Fig. 3).

Liquid then accumulates at the edge (rim) of the lamella and its thickness increases with time during the spreading and receding phases.

At the maximum spread the major driving forces become capillary forces. The droplet begins to recede because the surface is hydrophobic. Figure 11 shows the simulated shapes of the droplet during the receding phase. A very good agreement is obtained between the experiment and the simulation.

Note that in the later spreading stage, near the maximum spreading diameter, circumferential instability and fingering of the rim are visible and the axisymmetry is no longer maintained. Moreover, at large times t the amplitude of the waves is comparable with the drop diameter. This leads to the scatter of experimental data for the spread factor at the later stages of the drop impact.

At some time instant the rim merges and the inertia of the flow in the drop leads to the appearance of the uprising central jet. Such a jet at $t = 11$ ms is shown in Fig. 11. The asymmetric shape of the jet (left image) cannot be obtained by the simulations based on the axisymmetric numerical scheme (right).

Some numerical simulations show an air bubble entrapped near the impact point, which is usually also the origin of the coordinate system (see the light spot in the simulation results at times larger than 0.6 ms in Figs. 10 and 11). In the considered cases, it is not immediately clear whether this bubble is a numerical artifact associated with the VOF method or whether it is physical. In the volume-of-fluid method the drop/gas interface has a thickness comparable with the mesh size. It is defined using a so-called "color

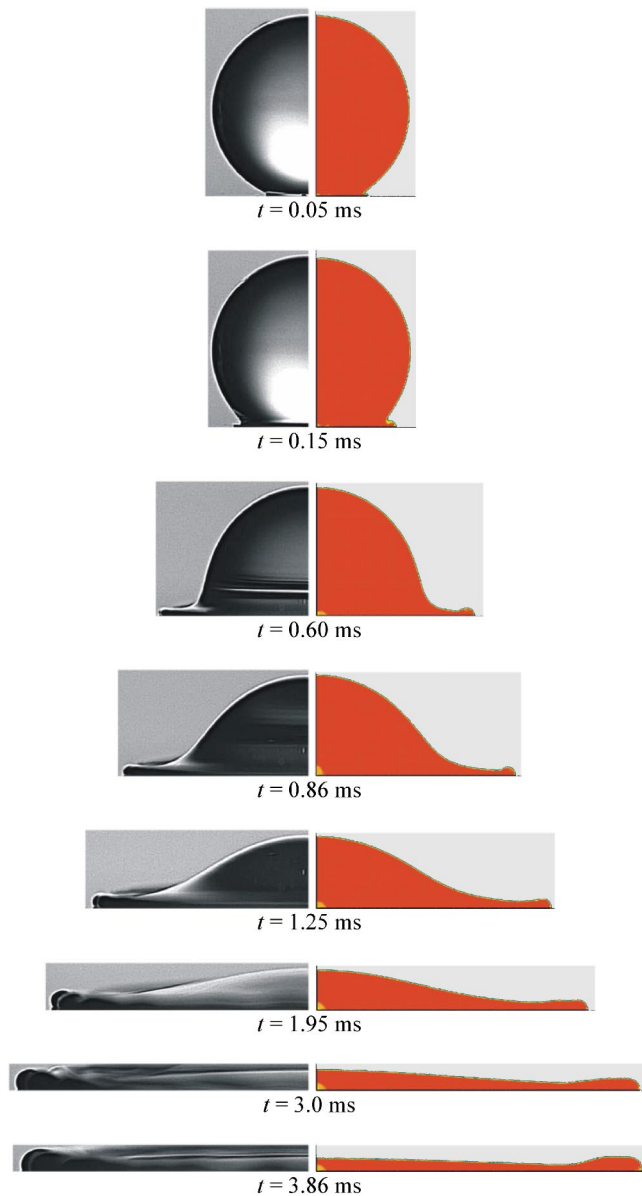


FIG. 10. (Color online). Time sequence of water drop impact onto a wax surface. Comparison of the simulation (right) and experiment (left) during the spreading phase. The impact parameters correspond to expt. 7 from Table II.

function” whose value varies between 1 (corresponding to the liquid phase) and 0 (corresponding to the ambient gas phase). The theoretical flow³⁹ in the corner during spreading, shown in Fig. 4(c), demonstrates also the possible numerical convection of the color function from the free liquid/gas interface to the liquid/wall surface along the streamlines. Such convection could lead to the collection of the gas phase on the substrate in the form of one or several bubbles. On the other hand, such entrapped bubbles have indeed been sometimes observed in experiments. In Fig. 12(a) an experimentally observed air bubble, in the form of a ring, is shown at a very initial stage of drop impact. The level of the surface is also shown to separate the drop image from the reflected picture. The dry area inside this ring-shaped air/solid contact area decreases sharply with time⁵² and quickly forms an air bubble inside the droplet, which can often be observed at

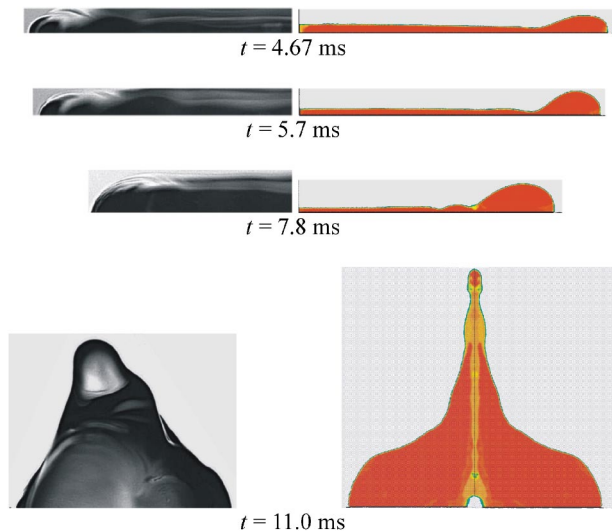


FIG. 11. (Color online). Time sequence of water drop impact onto a wax surface. Comparison of the simulation (right) and experiment (left) during the receding phase. The impact parameters correspond to expt. 7 from Table II.

later stages of the spreading phase [Fig. 12(b)]. The mechanism of the air bubble entrapment is already understood.⁵³ Such a bubble is formed because of the deformation of the drop surface prior to impact.

In the present study of axisymmetric drop impact, the bubble is formed in the stagnation region. Its size is much smaller than the drop diameter. Therefore, the influence of the bubble formation and its deformation (or probable numerical artifact) on the drop spreading is negligibly small.

The value of the apparent dynamic contact angle θ_D is calculated from the approximation of the shape of the drop, averaging the angle in the six cells in the neighborhood of the contact line (two horizontal rows adjacent to the wall, each row is of three cells). The results of calculations of θ_D are shown in Figs. 5(a) and 6 as a solid line. This calculated apparent contact angle includes the influence of the outer velocity field and therefore differs from the contact angle in the inner region, estimated by Hoffman’s law (5). The calculations of the apparent contact angle predict rather well the experimentally obtained values, in spite of the fact that the mesh size is not necessary comparable with the characteristic size of observations (corresponding to 1 pixel of the image). This agreement indicates that the phenomena near the con-

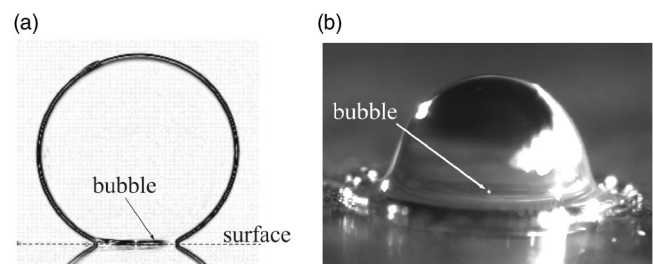


FIG. 12. Observations of air entrainment during drop impact: (a) the ring-shaped bubble at the very first stage of drop deformation and (b) small bubble in the stagnation region of the spreading drop.

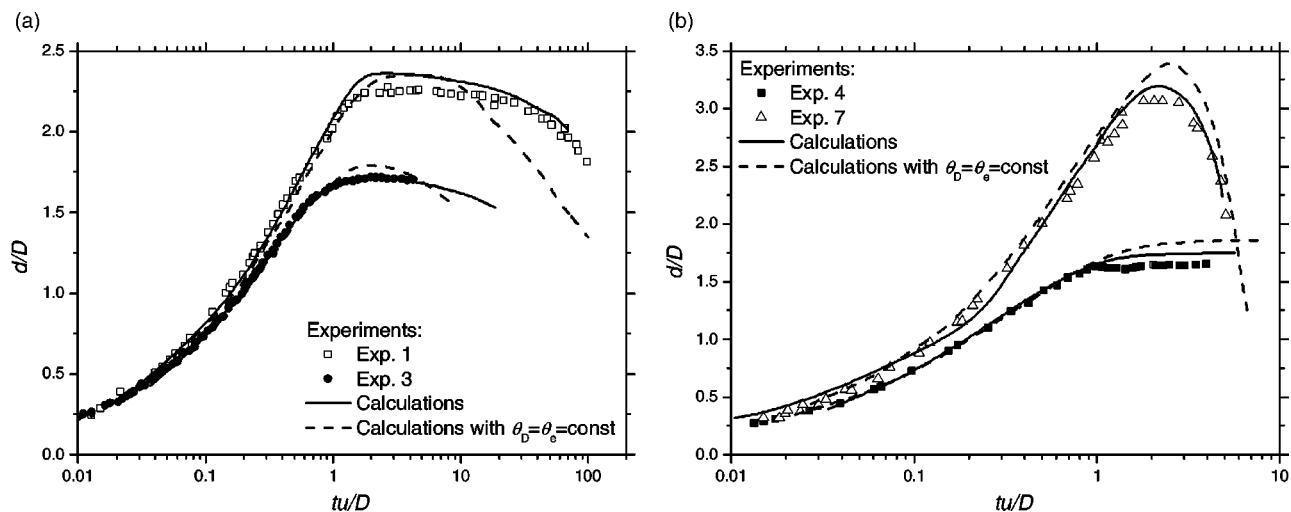


FIG. 13. Numerical calculations of the temporal evolution of the spread diameter in comparison with the experimental data and with the calculations with the assumed constant contact angle. The impact parameters correspond to (a) expt. 1 and expt. 3, and (b) expt. 4 and expt. 7 from Table II.

tact line are indeed governed by the inertial forces and can be calculated if the boundary conditions are accounted for correctly.

The experimental and numerical results for the spreading factor are shown in Fig. 13 for various impact parameters. These parameters correspond to the axisymmetric drop spreading without rim fingering and breakup. During such spreading the typical sizes of the capillary waves, appeared on the drop free surface (and clearly seen in Figs. 10 and 11), are negligibly small in comparison with the rim size, and the contact line can always be well approximated by a circle.

In this figure the experimental data for the spreading factor d/D are compared with the numerical predictions. In order to validate the model and to check the sensitivity of the numerical method, two types of the boundary conditions at the contact line are implemented in the numerical code. The continuous lines correspond to the numerical predictions using the proposed code in which the variable dynamic contact angle is calculated using (5). The dashed lines correspond to the calculations based on the assumption of the constant contact angle $\theta_D = \theta_a$ during the spreading phase and constant $\theta_D = \theta_r$ during the receding phase. The numerical code employing both types of the contact angle treatment predicts well the spreading factor in the early advancing phase, when the inertial effects are dominant and the influence of forces associated with wettability is small. During the receding phase of drop deformation the effects associated with the viscous drag in the inner region are significant. This is the reason why at the later stages of drop spreading and receding the results obtained with the proposed algorithm, based on the variable dynamic contact angle, agree much better with the experimental data than the code with the assumed constant θ_D .

In addition to the results shown in Fig. 13, several alternative tests of the numerical code with various boundary conditions at the contact line have been performed. Particularly, the values of the experimentally observed apparent contact angle have been used in the code. As expected, the predictions of the spread factor in these simulations have

shown a poor agreement with the experimental data (not shown here). The source of this disagreement is in the double accounting for the inertial effects in the corner: first they are taken into account in the value of the apparent contact angle and second they are introduced by the numerical code. Therefore, in the proposed approach the model for the dynamic contact angle must be inertialess, like the correlation (5). Use of theoretical models accounting for inertial effects (such as Ref. 51) in the code can lead to an increased error.

It should be noted that the values of the static advancing and receding contact angles, θ_a and θ_r , are properties of the combination liquid/gas/solid. They are measured in our experiments. Hence, the numerical model does not use any adjustable parameter.

V. CONCLUSION

There are two main conclusions of this study. First, the apparent dynamic contact angle is not only a function of the contact line speed but also a function of the flow field in the vicinity of the moving contact line.³⁷ For the drop impact the contact angle decreases to a minimum value and increases to a maximum value in the spreading phase, while the spread factor increases monotonically and thus the contact-line velocity decreases monotonically [see Fig. 5(a)]. In the subsequent recoiling phase the contact angle decreases to another minimum and again increases to the equilibrium state on wax while the spread factor decreases monotonically, hence the contact-line (receding) velocity decreases monotonically. On the glass surface the apparent dynamic contact angle in the recoiling phase decreases from a maximum to the final state while the spread factor remains constant and the contact-line velocity is zero [see Fig. 5(b)]. Therefore, a unique functional dependence of the apparent dynamic contact angle on the contact-line speed cannot be obtained to explain experimental results. Second, there is no effect of the static contact angle on the apparent dynamic contact angle over a large range of experimental data for the impact of a glycerin drop-

let. This is observed in the spreading stage where the inertia and viscous forces dominate the deformation.

As is seen from the comparison of the numerical results with the experimental data, assuming a fixed contact angle (advancing or receding) as one of the boundary conditions has obvious limitations. Such numerical simulations predict the spreading of the drop well; however, not the receding phase.

The numerical simulations calculate the velocity field in the outer region far from the contact line. On the other hand, existing theoretical/empirical expressions are valid for the small inner region of the contact line moving at small capillary number. These models do not account for the inertial effects in the outer flow. The proposed combined method allows a match of the computational results in the outer region with the theoretical/empirical expressions for the contact angle in the inner region. Such an algorithm improves significantly the agreement with experiment. It also predicts well the shape of the drop, the spread factor, and even the apparent contact angle during drop spreading and receding.

The phenomena of drop impact are frequently not axisymmetric, obviously in the case of inclined impact, but even if the impact velocity is normal to the wall surface. The rim instability and capillary waves are usual phenomena following the drop impact and spreading. These three-dimensional phenomena sometimes lead to the rim fingering, breakup, nonsymmetric shape of the uprising central jet (see Figs. 10 and 11). Simulation of these cases requires a 3D numerical code. The implementation of the proposed method of the apparent dynamic contact angle description in a three-dimensional code is a nontrivial but rather straightforward task.

ACKNOWLEDGMENTS

The authors would like to thank the DAAD (Deutscher Akademischer Austauschdienst) for supporting Š.Š. through a research fellowship and the DFG (Deutsche Forschungsgemeinschaft) for support through Project Nos. Tr194/10 and Tr194/12. The authors would like also to thank Dr. S. Muzafertija for making COMET available and discussing its use and some computational issues. The authors thank Professor S. Chandra and Professor S. Zaleski for discussions.

¹M. Rein, "Phenomena of liquid drop impact on solid and liquid surfaces," *Fluid Dyn. Res.* **12**, 61 (1993).

²S. Chandra and C. T. Avedisian, "On the collision of a droplet with a solid surface," *Proc. R. Soc. London, Ser. A* **432**, 13 (1991).

³A. Frohn and N. Roth, *Dynamics of Droplets* (Springer, Berlin, 2000).

⁴*Drop-Surface Interactions*, edited by M. Rein (Springer, Berlin, 2000).

⁵O. G. Engel, "Water drop collision with solid surfaces," *J. Res. Natl. Bur. Stand.* **54**, 281 (1953).

⁶Z. Levin and P. V. Hobbs, "Splashing of water drops on solid and wetted surfaces: Hydrodynamics and charge separation," *Philos. Trans. R. Soc. London, Ser. A* **269**, 555 (1971).

⁷C. D. Stow and M. G. Hadfield, "An experimental investigation of fluid flow resulting from the impact of a water drop with unyielding dry surface," *J. Meteorol. Soc. Jpn.* **55**, 518 (1980).

⁸C. Mundo, M. Sommerfeld, and C. Tropea, "Droplet-wall collisions: Experimental studies of the deformation and breakup process," *Int. J. Multiphase Flow* **21**, 151 (1995).

⁹G. E. Cossali, A. Coghe, and M. Marengo, "The impact of a single drop on a wetted solid surface," *Exp. Fluids* **22**, 463 (1997).

¹⁰K. Range and F. Feuillebois, "Influence of surface roughness on liquid drop impact," *J. Colloid Interface Sci.* **203**, 16 (1998).

¹¹R. Rioboo, M. Marengo, and C. Tropea, "Outcomes from a drop impact on solid surfaces," *Atomization Sprays* **11**, 155 (2001).

¹²A. M. Worthington, "On the forms assumed by drops of liquids falling vertically on a horizontal plate," *Proc. R. Soc. London* **25**, 261 (1876).

¹³G. S. Hartley and R. T. Brunskill, "Reflection of water drops from surfaces," *Surface Phenomena in Chemistry and Biology* (Pergamon, Oxford, 1958), Vol. 57, p. 214.

¹⁴R. E. Ford and C. G. L. Furmidge, "Impact and spreading of spray drops on foliar surfaces," *Wetting* (Society of Chemical Industry Monograph, London, 1967), Vol. 25, p. 417.

¹⁵J. Fukai, Y. Shiiba, T. Yamamoto, O. Miyatake, D. Poulikakos, C. M. Megaridis, and Z. Zhao, "Wetting effects on the spreading of a liquid droplet colliding with a flat surface: experiment and modeling," *Phys. Fluids* **7**, 236 (1995).

¹⁶M. Pasandideh-Fard, Y. M. Qiao, S. Chandra, and J. Mostaghimi, "Capillary effects during droplet impact on a solid surface," *Phys. Fluids* **8**, 650 (1996).

¹⁷T. Mao, D. C. S. Kuhn, and H. Tran, "Spread and rebound of liquid droplets upon impact on flat surfaces," *AIChE J.* **43**, 2169 (1997).

¹⁸R. Rioboo, M. Marengo, and C. Tropea, "Time evolution of liquid drop impact onto solid, dry surfaces," *Exp. Fluids* **33**, 112 (2001).

¹⁹I. V. Roisman, R. Rioboo, and C. Tropea, "Normal impact of a liquid drop on a dry surface: Model for spreading and receding," *Proc. R. Soc. London, Ser. A* **458**, 1411 (2002).

²⁰I. V. Roisman, B. Prunet-Foch, C. Tropea, and M. Vignes-Adler, "Multi-phase drop impact onto a dry substrate," *J. Colloid Interface Sci.* **256**, 396 (2002).

²¹F. H. Harlow and J. P. Shannon, "The splash of a liquid drop," *J. Appl. Phys.* **38**, 257 (1967).

²²J. Fukai, Z. Zhao, D. Poulikakos, C. M. Megaridis, and O. Miyatake, "Modeling of the deformation of a liquid droplet impinging upon a flat surface," *Phys. Fluids A* **5**, 2588 (1993).

²³A. Karl, M. Rieber, M. Shelkle, K. Anders, and A. Frohn, "Comparison of new numerical results for droplet wall interactions with experimental results," *Proceedings of the ASME Fluid Engineering Division Summer Meeting*, edited by H. Coleman *et al.* (San Diego, 1996), Vol. 1, p. 202–206.

²⁴A. Karl, K. Anders, M. Rieber, and A. Frohn, "Deformation of liquid droplets during collisions with hot walls: Experimental and numerical results," *Part. Part. Syst. Charact.* **13**, 186 (1996).

²⁵D. A. Weiss and A. Yarin, "Single drop impact onto liquid films: Neck distortion, jetting, tiny bubble entrainment, and crown formation," *J. Fluid Mech.* **385**, 229 (1999).

²⁶M. Bussmann, J. Mostaghimi, and S. Chandra, "On a three-dimensional volume tracking model of droplet impact," *Phys. Fluids* **11**, 1406 (1999).

²⁷M. Bussmann, S. Chandra, and J. Mostaghimi, "Modeling the splash of a droplet impacting a solid surface," *Phys. Fluids* **12**, 3121 (2000).

²⁸C. Josserand and S. Zaleski, "Droplet splashing on a thin liquid film," *Phys. Fluids* **15**, 1650 (2003).

²⁹P. R. Gunjal, V. V. Ranade, and R. V. Chaudhari, "Dynamics of drop impact on solid surface: Experiments and VOF simulations," *AIChE J.* **51**, 59 (2005).

³⁰C. W. Hirt and B. D. Nichols, "Volume of fluid (VOF) method for the dynamics of free boundaries," *J. Comput. Phys.* **39**, 201 (1981).

³¹D. T. Blake and J. K. Ruschak, "Wetting: Static and dynamic contact lines," in *Liquid Film Coating*, edited by F. S. Kistler and M. P. Schweizer (Chapman and Hall, London, 1997), pp. 63–97.

³²Y. D. Kwok and W. A. Neumann, "Contact angle measurement and contact angle interpretation," *Adv. Colloid Interface Sci.* **81**, 167 (1999).

³³Y. D. Shikhmurzaev, "The moving contact line on a smooth solid surface," *Int. J. Multiphase Flow* **19**, 589 (1993).

³⁴Y. D. Shikhmurzaev, "Dynamic contact angles in gas/liquid/solid systems and flow in vicinity of moving contact line," *AIChE J.* **42**, 601 (1996).

³⁵Y. D. Shikhmurzaev, "Moving contact lines in liquid/liquid/solid systems," *J. Fluid Mech.* **334**, 211 (1997).

³⁶Y. D. Shikhmurzaev, "Spreading of drops on solid surfaces in a quasi-static regime," *Phys. Fluids* **9**, 266 (1997).

³⁷T. D. Blake, M. Bracke, and Y. D. Shikhmurzaev, "Experimental evidence of nonlocal hydrodynamic influence on the dynamic contact angle," *Phys. Fluids* **11**, 1995 (1999).

³⁸R. G. Cox, "The dynamics of the spreading of liquids on a solid surface. Part 1. Viscous flow," *J. Fluid Mech.* **168**, 169 (1986).

- ³⁹H. K. Moffat, "Viscous and resistive eddies near a sharp corner," *J. Fluid Mech.* **18**, 1 (1964).
- ⁴⁰R. L. Hoffman, "A study of the advancing interface. I. Interface shape in liquid-gas systems," *J. Colloid Interface Sci.* **50**, 228 (1975).
- ⁴¹T. Jiang, S. Oh, and J. C. Slattery, "Correlation for dynamic contact angle," *J. Colloid Interface Sci.* **69**, 74 (1979).
- ⁴²M. Bracke, F. De Voeght, and P. Joos, "The kinematics of wetting: The dynamic contact angle," *Prog. Colloid Polym. Sci.* **79**, 142 (1989).
- ⁴³J. E. Seebergh and J. C. Berg, "Dynamic wetting in the low capillary number regime," *Chem. Eng. Sci.* **47**, 4455 (1992).
- ⁴⁴S. F. Kistler, "Hydrodynamics of wetting," in *Wettability*, edited by J. C. Berg (Marcel Dekker, New York, 1993), p. 311.
- ⁴⁵Š. Šikalo, M. Marengo, C. Tropea, and E. N. Ganić, "Analysis of droplet impact on horizontal surfaces," *Exp. Therm. Fluid Sci.* **25**, 503 (2002).
- ⁴⁶S. Muzaferija and M. Perić, "Computations of free surface flows using interface-tracking and interface-capturing methods," in *Nonlinear Water Wave Interaction*, edited by O. Mahrenholtz and M. Markiewicz (WIT Press, Southampton, 1998).
- ⁴⁷J. U. Brackbill, D. B. Kothe, and C. Zemach, "A continuum method for modeling surface tension," *J. Comput. Phys.* **100**, 335 (1992).
- ⁴⁸*COMET User Manual*, Institute of Computational Continuum Mechanics GmbH, Hamburg, Germany (February 1998).
- ⁴⁹M. Rieber and A. Frohn, "A numerical study of the mechanism of splashing," *Int. J. Heat Fluid Flow* **20**, 455 (1999).
- ⁵⁰T. D. Blake, "Dynamic contact angles and wetting kinetics," in *Wettability*, Surfactant Science Series, edited by J. C. Berg (Marcel Dekker, New York, 1993), Vol. 49, p. 251.
- ⁵¹R. G. Cox, "Inertial and viscous effects on dynamic contact angles," *J. Fluid Mech.* **357**, 249 (1998).
- ⁵²H. Fujimoto, H. Shiraishi, and N. Hatta, "Evolution of liquid/solid contact area of a drop impinging on a solid surface," *Int. J. Heat Mass Transfer* **43**, 1673 (2000).
- ⁵³V. Mehdi-Nejad, J. Mostaghimi, and S. Chandra, "Air bubble entrapment under an impacting droplet," *Phys. Fluids* **15**, 173 (2003).